

Article

A High Precision Capacitive Linear Displacement Sensor with Time-Grating That Provides Absolute Positioning Capability Based on a Vernier-Type Structure

Xiaokang Liu ¹, Hui Zhang ², Kai Peng ^{1,*}, Qifu Tang ¹ and Ziran Chen ¹

¹ Engineering Research Center of Mechanical Testing Technology and Equipment (Ministry of Education), Chongqing University of Technology, Chongqing 400054, China; lxx@cqut.edu.cn (X.L.); tqf@cqut.edu.cn (Q.T.); czr@cqut.edu.cn (Z.C.)

² School of Electrical and Electronic Engineering, Chongqing University of Technology, Chongqing 400054, China; ZHandLCL@126.com

* Correspondence: pkgogo1987@163.com; Tel.: +86-023-6256-3387

Received: 31 October 2018; Accepted: 26 November 2018; Published: 28 November 2018



Abstract: Nanometer-scale measurement devices with high accuracy and absolute long-range positioning capability are increasingly demanded in the field of computer numerical control machining. To meet this demand, the present report proposes a capacitive absolute linear displacement sensor with time-grating that employs a vernier-type structure based on a previously proposed single-row capacitive sensing structure. The novel proposed vernier-type absolute time-grating (VATG) sensor employs two capacitor rows, each with an equivalent measurement range. The first capacitor row is designed with n periods to realize fine measurement, while the second capacitor row is designed with $n - 1$ periods, and the phase difference between the second row and the first row is employed to obtain absolute positioning information. A prototype VATG sensor with a total measurement range of 600 mm and $n = 150$ is fabricated using printed circuit board manufacturing technology, and its measurement performance is evaluated experimentally. Harmonic analysis demonstrates that the measurement error mainly consists of first-harmonic error, which is mostly caused by signal crosstalk. Accordingly, an optimized prototype VATG sensor is fabricated by adding a shielding layer between the two capacitor rows and designing a differential induction structure. Experimental results demonstrate that the measurement error of the optimized prototype sensor is $\pm 1.25 \mu\text{m}$ over the full 600 mm range and $\pm 0.25 \mu\text{m}$ over a single 4 mm period.

Keywords: capacitive linear displacement sensor; vernier-type absolute structure; differential sensing structure; time-grating

1. Introduction

Absolute position displacement measurement sensors play an irreplaceable role in the field of high-precision measurements and as a component in the closed loop feedback control of computer numerical control (CNC) machine tool systems. The rapid development of high-precision positioning technology in CNC machine tool systems has generated an increasing demand for robust absolute displacement measurement sensors with high positioning accuracy and excellent repetitive positioning precision in harsh environments, such as under the conditions of electromagnetic interference, mechanical vibration, extreme temperature variation, and dust contamination [1–7]. Meanwhile, many types of absolute grating displacement measurement sensors with high precision

and high resolution have been developed, including capacitive grating sensors [1,2], magnetic grating sensors [8], and optical grating sensors [9].

Absolute optical grating (AOG) sensors are based on an evaluation of the intensity of incident light from a known illumination source, and represent an efficient means for conducting closed loop position control in CNC machine tool systems [10–13]. The measurement error of AOG sensors has been reduced to values as small as $\pm 0.275 \mu\text{m}$ over a 10 mm range and $\pm 5 \mu\text{m}$ over a full 3040 mm range. However, mechanical vibration, temperature variation, and dust contamination affect the light intensity and other characteristics of the illumination source incident on the sensor, all of which detract from the measurement performance of AOG sensors. It has a weak anti-interference capability, particularly in the harsh environments associated with many CNC machining applications [13,14].

In contrast to AOG sensors, both magnetic and capacitive grating sensors have high tolerance for mechanical vibration and contamination due to dust and oil and, therefore, are commonly employed in servo drive systems [2,8,15]. The measurement error of absolute magnetic grating sensors can achieve values as low as $\pm 5 \mu\text{m}$ over a 1000 mm range and can obtain a measurement resolution of $0.75 \mu\text{m}$ [15–17]. However, the large size of the magnetic head and poor resistance to electromagnetic interference restrict the use of such sensors for high accuracy applications. In comparison, capacitive grating sensors provide a fuller range of environmental advantages, which make them ideally suited to harsh machining environments [2,18–21]. Moreover, the measurement error of absolute capacitive grating sensors can achieve values as low as $\pm 0.3 \mu\text{m}$ over a 6 mm range, with an error of less than 0.01% over the full measurement range [2]. However, the measurement range of absolute capacitive grating sensors is limited, which restricts their use in practical applications [2].

The present work addresses the limitations of absolute capacitive grating sensors by developing a novel capacitive absolute linear displacement sensor that employs a vernier-type structure with time-grating based on a previously proposed single-row capacitive sensing structure [22]. The proposed vernier-type absolute time-grating (VATG) sensor employs two capacitor rows. According to the design of vernier calipers, the auxiliary scale, or vernier scale, includes n gradations over the total caliper length, while the main scale includes $n - 1$ gradations over the same total caliper length. Similarly, one capacitor row of the VATG sensor is composed of n periods over the total sensor length and serves as a fine measurement scale to ensure high measurement resolution, which is analogous to the auxiliary scale of vernier calipers. The other row of the VATG sensor is composed of $n - 1$ periods over the total sensor length as a coarse measurement scale used to find the phase difference of two rows to realize absolute positioning, which is analogous to the main scale of vernier calipers. A prototype VATG sensor is fabricated using printed circuit board (PCB) manufacturing technology with a capacitor row composed of 150 periods to realize fine measurement, and the second capacitor row composed of 149 periods to realize course measurement. Based on an analysis of the measurement performance of the prototype VATG sensor, the design is optimized by increasing the distance between the two rows and adding a shielding layer between them to reduce the influence of signal crosstalk, and a differential induction structure is adopted to eliminate common-mode interference, which significantly improves the measurement performance of the modified prototype VATG sensor. The remainder of this paper is organized as follows. Section 2 introduces the structures and measurement principles of the single-row capacitive sensor and the proposed VATG sensor. Section 3 presents an analysis of the limit of error of the VATG sensor. The experimental results and optimization methodology are presented and discussed in Section 4. Finally, Section 5 presents the main conclusions of the work.

2. Sensor Structure and Measurement Principle

2.1. Single-Row Sensor Measurement Principle

The structure of the single-row capacitive displacement sensor is illustrated in Figure 1a. The sensing structure consists of independent plate capacitor arrays, where the sequence of four adjacent rectangular

excitation electrodes labeled $S+$, $C+$, $S-$, and $C-$ are fixed in stationary positions to provide a small period of W . Four orthogonal sinusoidal AC excitation signals of amplitude A and angular frequency ω , denoted as $U_{S+} = A_m \sin(\omega t)$, $U_{C+} = A_m \cos(\omega t)$, $U_{S-} = -A_m \sin(\omega t)$, and $U_{C-} = -A_m \cos(\omega t)$ are respectively applied to the electrodes labeled $S+$, $C+$, $S-$, and $C-$. Here, the length of the excitation electrodes in the y direction is H and the width is $(W/4 - l)$, where l is the interval between two adjacent excitation electrodes in the x direction. The stationary excitation electrodes are overlaid by an array of sinusoidal-shaped induction electrodes of length H and maximum width $W/2$ that are movable in the x direction and have relative positions fixed with a periodicity of W , where the interval between two adjacent induction electrodes in the x direction is $W/2$. As illustrated in Figure 1b, the moveable induction electrodes are aligned parallel with the stationary excitation electrodes with a distance of separation d_0 in the z direction. The sequence of four excitation electrodes labeled $S+$, $C+$, $S-$, and $C-$ and one induction electrode thereby form four planar capacitors with capacitance values denoted as C_1 , C_3 , C_2 , and C_4 , respectively. In addition, the values of C_1 and C_3 , and C_2 and C_4 vary oppositely as the induction electrode moves along the x axis, as illustrated by the equivalent circuit shown in Figure 1d. Here, R represents load resistance. According to the superposition theorem of the equivalent circuit, the output U_o is obtained as

$$U_o = U_{S+} \frac{Z_{L1}}{Z_{L1} + Z_1} + U_{S-} \frac{Z_{L3}}{Z_{L3} + Z_3} + U_{C+} \frac{Z_{L2}}{Z_{L2} + Z_2} + U_{C-} \frac{Z_{L4}}{Z_{L4} + Z_4}, \tag{1}$$

where $Z_{Lj} = -1 / (\sum_{i=1}^4 \frac{1}{C_i} + \frac{1}{R})$ is equivalent capacitive-reactance for $i \neq j, j = 1, 2, 3, 4$, when $S+$, $C+$, $S-$, and $C-$ work in dependence; Z_1, Z_2, Z_3 and Z_4 are the capacitive-reactance of C_1, C_2, C_3 , and C_4 , changing with the movement of the moveable induction electrodes owing to the variation of the value of C_1, C_2, C_3 , and C_4 . Thus, the final output can be given as follows [22]:

$$U_o = \frac{U_{S+} \Delta S_{S+}}{2S_0} + \frac{U_{S-} \Delta S_{S-}}{2S_0} + \frac{U_{C+} \Delta S_{C+}}{2S_0} + \frac{U_{C-} \Delta S_{C-}}{2S_0}, \tag{2}$$

where the value $S_0 = (HW/\pi) \cos(\pi l/W)$ represents the maximum area of overlap between an excitation electrode and an induction electrode, and $\Delta S_{S+}, \Delta S_{C+}, \Delta S_{S-}$, and ΔS_{C-} are the efficient variations in the overlapping area between the $S+, C+, S-$, and $C-$ excitation electrodes and a single induction electrode, respectively, when d_0 and the dielectric coefficient ϵ_0 remain constant. However, Figure 1a,c illustrates the case where the sinusoidal-shaped induction electrode moving along the x axis with respect to the stationary rectangular excitation electrodes can be equivalent to a rectangular induction electrode moving along the x axis with respect to a set of four stationary half-sinusoidal-shaped excitation electrodes if the single-row sensing structure is divided into two halves along the x axis. Here, the latter case can be regarded as an uncertain limit integral of a cosine or sine function [3,21–24]. Therefore, the effective area variation ΔS can be formulated according to the displacement x along the x direction as follows [22]:

$$\begin{aligned} \Delta S_{S+} &= \frac{WH}{\pi} (1 - \cos \frac{2\pi x}{W}), & \Delta S_{S-} &= \frac{WH}{\pi} (1 + \cos \frac{2\pi x}{W}), \\ \Delta S_{C+} &= \frac{WH}{\pi} (1 + \sin \frac{2\pi x}{W}), & \Delta S_{C-} &= \frac{WH}{\pi} (1 - \sin \frac{2\pi x}{W}). \end{aligned} \tag{3}$$

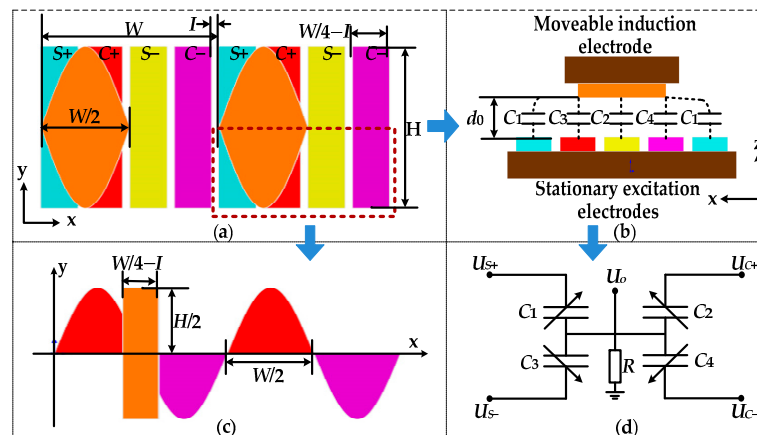


Figure 1. Schematic diagrams of a single-row capacitive displacement sensing structure and its measurement principle. Top view (a) and side view (b) schematic diagrams of the single-row sensing structure. (c) Schematic diagram presents a geometric representation of the effective area variation of the selected region in (a). (d) Equivalent capacitor circuit based on (b).

Thus, the final output is given as follows:

$$U_o = A \sin\left(\omega t - \frac{2\pi x}{W}\right), \tag{4}$$

where A is the coupling coefficient, and U_o is a travelling wave signal whose frequency and amplitude are determined by the excitation signals U_{S+} , U_{C+} , U_{S-} , and U_{C-} , but its phase varies proportionately with respect to x , and changes with a periodicity of W . Because the travelling wave signal represents a relationship between the spatial displacement and a time standard, we express the output as follows:

$$U_o = A \sin\left(\frac{2\pi}{T} t - \frac{2\pi x}{W}\right), \tag{5}$$

where T is the time period of the travelling wave signal determined by the excitation signals. Accordingly, a single-row capacitive structure cannot obtain absolute position measurements without first knowing the starting position. However, absolute position measurements can be obtained by adopting a double-row capacitive structure.

2.2. Absolute Measurement Principle

The double-row capacitive structure of the VATG sensor is illustrated in Figure 2a, where stationary excitation electrodes serve as the stator, and moveable induction electrodes serve as the mover. Here, the stator consists of two-row stationary excitation electrodes, and each row occupies an equivalent overall length of L . In the same way, the mover consists of two-row corresponding inductive electrodes, and each row occupies an equivalent length of $L/12$. Meanwhile, a multilayer thin-film sensing structure is employed, where the electrodes and the lead wires are separated by a thin-film insulating layer, and the electrodes and lead wires are connected by a connecting column.

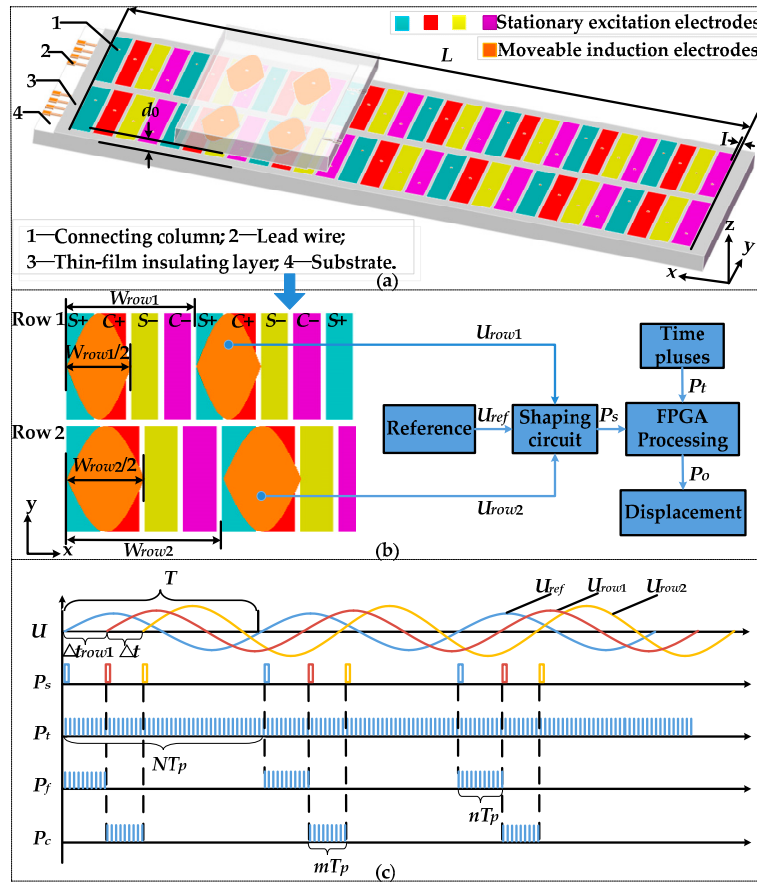


Figure 2. (a) Schematic diagram of a double-row Vernier-type capacitive structure for conducting absolute position measurements with time-grating. (b) Schematic diagram illustrating the absolute position measurement principle of double-row capacitive structure. (c) High-frequency clock pulse interpolation.

As shown in Figure 2b, the VATG sensor includes two single-row capacitive sensing structures denoted as row 1 and row 2 with different periodicities of W_{row1} and W_{row2} , respectively. Because the value of I is equivalent for both rows, the widths of the excitation electrodes in row 1 and row 2 are $(W_{row1}/4 - I)$ and $(W_{row2}/4 - I)$, respectively. In addition, L/W_{row1} and L/W_{row2} are both integers, and $L/W_{row1} - L/W_{row2} = 1$. According to (5), the corresponding output voltage signals U_{row1} and U_{row2} of row 1 and row 2 can be given as

$$U_{row1} = A_{row1} \sin\left(\frac{2\pi}{T}t - \frac{2\pi x}{W_{row1}}\right), U_{row2} = A_{row2} \sin\left(\frac{2\pi}{T}t - \frac{2\pi x}{W_{row2}}\right), \quad (6)$$

where A_{row1} and A_{row2} are coupling coefficients of row 1 and row 2, respectively. We then define a reference signal U_{ref} with an equivalent frequency as U_{row1} and U_{row2} . Accordingly, we can define the time difference Δt_{row1} along the time axis as representing the phase difference between U_{row1} and U_{ref} ; and the time difference Δt as representing the phase difference between U_{row1} and U_{row2} [25]. As shown in Figure 2b, U_{row1} , U_{row2} , and U_{ref} are routed to a shaping circuit to convert them into square wave signals. The respective rising edges of the square wave signals, which are collectively denoted as P_s for convenience, are then routed to a phase-comparing circuit constructed using a field-programmable gate array (FPGA). High-frequency clock pulses P_t with a period T_p are also input into the phase-comparing circuit as the time standard to interpolate Δt_{row1} and Δt . The interpolation process is illustrated in Figure 2c, where the rising edge of the converted U_{ref} initiates the counting of pulses P_f until the rising edge of the converted U_{row1} is encountered. Then, pulses P_c are counted until the next rising edge

of the converted U_{ref} is encountered after a total period T . Accordingly, if n pulses P_f are counted, $\Delta t_{row1} = nT_p$ to realize the fine measurement of row 1, and, if m pulses P_c are counted, $\Delta t = mT_p$ to realize the coarse measurement of row 2. We also note from Figure 2c that $T = NT_p$, and mT_p can be employed to calculate the number of periods, M , that the induction electrode array has moved relative to the stationary excitation electrodes as follows:

$$M = \text{int}\left(\left(\frac{mT_p}{NT_p}L\right)/W\right), \tag{7}$$

where the operator $\text{int}(\cdot)$ returns the integer value of its argument. Therefore, the relationship between x and Δt can be defined as follows:

$$x = W\left(M + \frac{\Delta t}{T}\right) = W\left(\text{int}\left(\left(\frac{m}{N}L\right)/W\right) + \frac{n}{N}\right), \tag{8}$$

Figure 3 presents the phase curves of U_{row1} and U_{row2} within their periods W_{row1} and W_{row2} with respect to displacement x obtained for $L = 60$ mm, $W_{row1} = 10$ mm, $W_{row2} = 12$ mm. According to Figure 3a, the phases of the two signals are distributed in a sawtooth form according to the value of x in each period. We also note that the phase curve of U_{row1} becomes increasingly advanced relative to that of U_{row2} with increasing x . Additionally, until $x = 600$ mm, the phase of row 2 differs by exactly a period from that of row 1. From Figure 3b, we note that the phase difference arising between the two signals with increasing x is monotonic and very nearly linear. As such, positioning can be realized according to the phase difference.

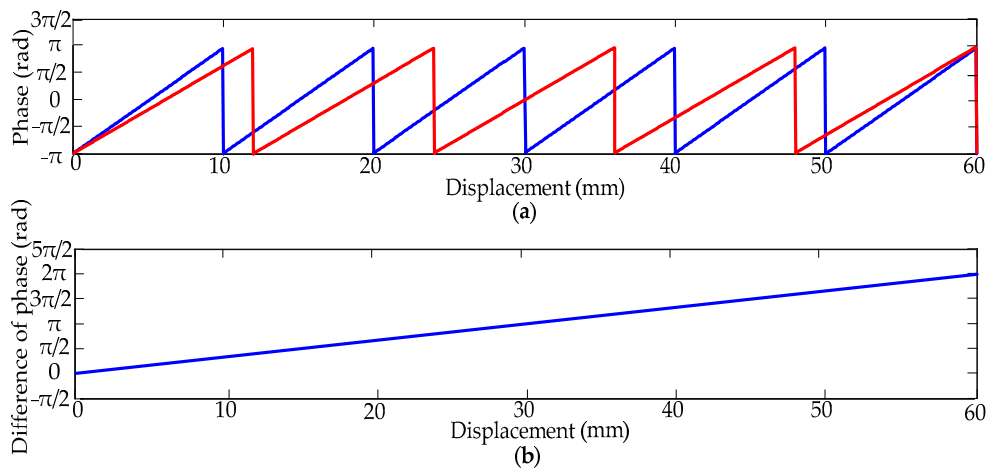


Figure 3. (a) Phase of outputs of row 1 (U_{row1}) and row 2 (U_{row2}) within their periods W_{row1} and W_{row2} , respectively, versus the displacement of the induction electrode array. (b) Phase difference with respect to the displacement of the induction electrode array.

3. Analysis of the Limit of Error

As discussed, row 1 and row 2 of the VATG sensor correspond to the auxiliary ruler and the main ruler of a vernier caliper, respectively. In a similar manner, we can denote the magnitude of a single scale division on row 2 of the VATG sensor (corresponding to the main ruler of a vernier caliper) as W_{row2} and the magnitude of a single scale division on row 1 (corresponding to the auxiliary ruler of a vernier caliper) as W_{row1} . Therefore, the limit of error of the VATG sensor is given as follows.

$$E_{limit} = W_{row2} - W_{row1}, \tag{9}$$

This relationship is illustrated in Figure 4. According to the measurement principle of the VATG sensor, the realization of absolute position measurement is defined completely according to E_{limit} , that is, $E < E_{limit}$, where E is the error in absolute position measurements.

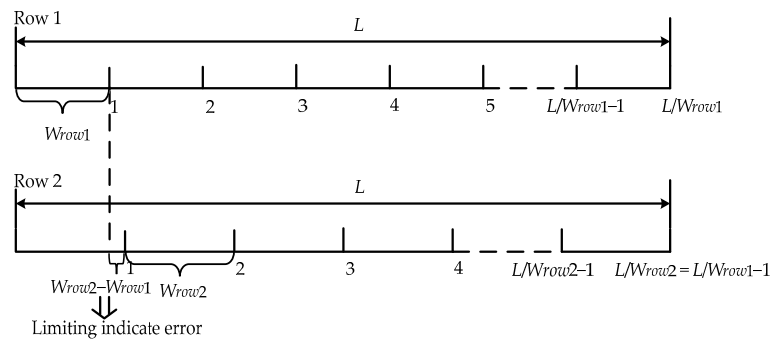


Figure 4. Schematic illustrating the determination of the limit of error for the proposed VATG sensor.

4. Results and Discussion

A prototype VATG sensor like that illustrated in Figure 2a was fabricated using PCB manufacturing technology with row 1 composed of $n = 150$ periods and row 2 composed of 149 periods, where the accuracy of PCB manufacturing technology can reach $10 \mu\text{m}$ [23]. The parameters of the sensor were $L = 600 \text{ mm}$, $W_{row1} = L/n = 600/150 = 4 \text{ mm}$, $W_{row2} = L/(n - 1) = (600/149) \approx 4.02684564 \text{ mm}$, and $E_{limit} = W_{row2} - W_{row1} \approx 26.845 \mu\text{m}$. The measurement performance of the VATG sensor was evaluated experimentally. The experimental setup is shown in Figure 5. It consists of an Aerotech ABL2000 air-bearing linear stage with a positioning accuracy of $\pm 1.5 \times 10^{-6}$ over a 120 mm traveling range, a Physik Instrumente H-824 6-axis miniature hexapod stage with a repeatability of $\pm 0.1 \mu\text{m}$, a Renishaw XL80 laser interferometer with a $\pm 0.5 \text{ ppm}$ precision as a measurement standard, a signal processing system, and a sensor loaded with shells. Here, the shell of the stator is 655 mm long, 37 mm wide, and 15 mm high, while that of the mover is 96 mm long, 37 mm wide, and 26 mm high. The stator was fixed on the air-bearing linear stage. The mover was mounted on the six-axis miniature hexapod stage for adjusting the relative spatial position between the excitation and induction electrodes with sub-micrometer precision, and maintaining a gap width $d_0 = 0.8 \text{ mm}$. As such, the stator was actually translated during the experiments, and the mover was held stationary. The data was acquired and processed by the signal processing system, and the results were compared with the data obtained from the laser interferometer.

The displacement measurement errors of the two rows of the prototype VATG sensor individually are shown in Figure 6a as a function of the displacement at 145 points along the entire 600 mm range of the sensor. Here, the error is observed to increase linearly with increasing displacement, and the minimum error is around $6.5 \mu\text{m}$. This type of error is characteristic of all sensors using a repeated periodic structure and that employ an incremental measurement method. However, the double-row capacitive structure can eliminate measurement error accumulated over a small period, as indicated by the measurement error of the prototype VATG sensor over the full range shown by the curve in Figure 6b obtained before optimization. Compared with the measurement errors of the single capacitive rows in Figure 6a, the measurement error has been reduced by $3 \mu\text{m}$ at least, and achieves a measurement error of $3.5 \mu\text{m}$ at most over the full displacement range, which is much less than the E_{limit} value of $26.845 \mu\text{m}$. Therefore, the prototype VATG sensor can realize absolute displacement measurements.

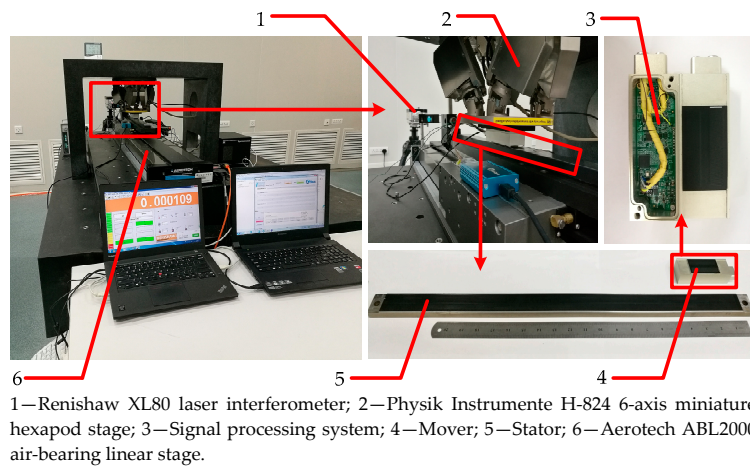


Figure 5. Experimental setup employed for evaluating the measurement performance of the prototype VATG sensors manufactured using printed circuit board technology.

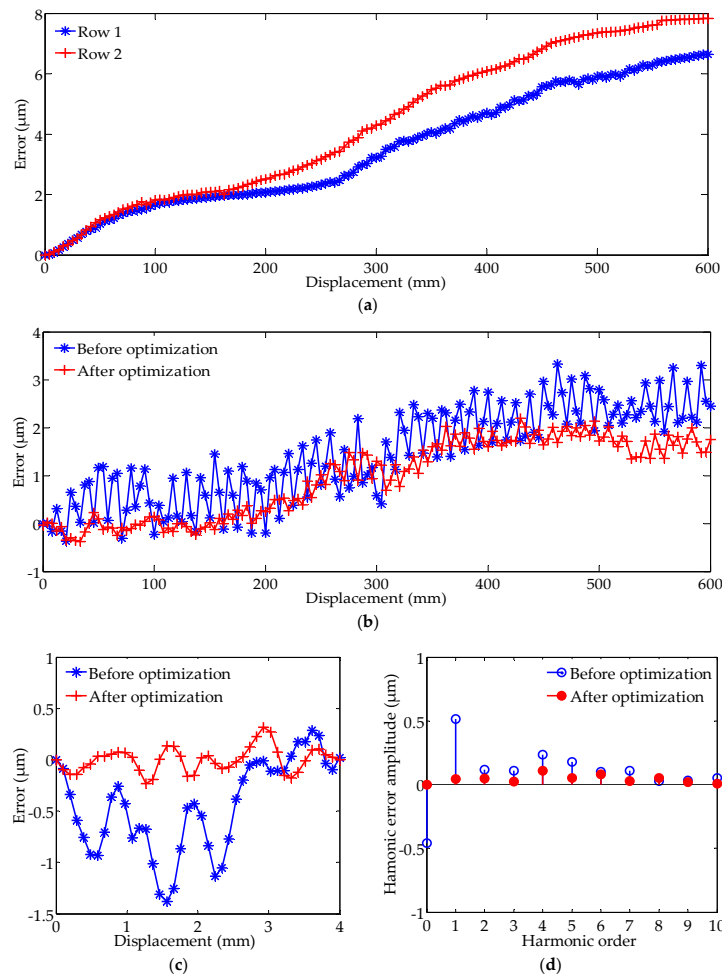


Figure 6. (a) Measurement errors of two rows of the initial prototype VATG sensor over the full measurement range. (b) Measurement errors of the VATG sensor obtained over the full measurement range before optimization and after optimization. (c) Measurement errors obtained over a single 4 mm period before optimization and after optimization. (d) Frequency spectra of measurement errors for a single 4 mm period before optimization and after optimization.

The measurement performance of the prototype VATG sensor was further evaluated by plotting the measurement error with respect to displacement taken at 42 points over a single 4 mm period. The results presented in Figure 6c before optimization demonstrate that the sensor exhibits a periodic measurement error of $\pm 0.75 \mu\text{m}$ over the single period. Figure 6d presents the results of harmonic analysis based on the fast Fourier transform of the periodic measurement error data obtained before optimization. The figure indicates that the primary harmonic component includes the first-order harmonic error component with an amplitude greater than $0.5 \mu\text{m}$ with much smaller fourth-order and fifth-order harmonic component contributions and relatively minor contributions from the remaining components. Here, the first-order harmonic error component is faintest because the experimental environment is controlled by high-precision instruments. However, physical non-uniformities in the four excitation electrode arrays, as well as non-uniformities in the electric fields of the electrodes, can introduce first-order harmonic error [24,25]. Moreover, non-uniformities in the electric fields of the electrodes can be exacerbated by signal crosstalk among the electrodes of two rows. That is to say, a certain quantity of excitation signals (briefly summarized as two types of excitation signals, sinusoidal and cosine signals) are introduced into the inductive output signal. To analyze the effect of crosstalk among electrodes on the measurement accuracy of the VATG sensor, we take row 1 as an example and consider the following mathematical model of a capacitive time-grating sensor.

$$\begin{aligned} U_{row1} &= A_{row1} \sin\left(\omega t - \frac{2\pi x}{W}\right) + \delta_1 \sin(\omega t) + \delta_2 \cos(\omega t) \\ &= A_{row1} \sin\left(\omega t - \frac{2\pi x}{W}\right) + \sqrt{\delta_1^2 + \delta_2^2} \sin\left(\omega t + \arctan\frac{\delta_2}{\delta_1}\right), \end{aligned} \tag{10}$$

where δ_1 and δ_2 are the relational coefficients of crosstalk signals caused by a certain quantity of excitation signals. Thus, signal crosstalk can result in first-order harmonic error. To address this issue, the VATG sensor design was optimized by increasing the distance between the two rows and adding a shielding layer between them to reduce the influence of signal crosstalk among the electrodes of two rows. In addition, we adopted a differential induction structure to reduce common mode disturbance. To analyze the effect of the differential induction structure for reducing common mode disturbance, the following mathematical model can be established.

$$\begin{aligned} U_{row1} &= \left[A_{row1} \sin\left(\omega t - \frac{2\pi x}{W}\right) + \delta'_1 \sin(\omega t) + \delta'_2 \cos(\omega t) \right] \\ &\quad - \left[A_{row1} \sin\left(\omega t - \frac{2\pi x}{W} + \pi\right) + \delta'_1 \sin(\omega t) + \delta'_2 \cos(\omega t) \right] \\ &= 2A_{row1} \sin\left(\omega t - \frac{2\pi x}{W}\right), \end{aligned} \tag{11}$$

where δ'_1 and δ'_2 are the relational coefficients of common mode disturbance caused by physical non-uniformities in the four excitation electrode arrays and by non-uniformities in the electric fields of the electrodes. These changes are illustrated in Figure 7.

A new prototype VATG sensor employing the optimized structure illustrated in Figure 7 was then fabricated, and its measurement performance was evaluated using the experimental setup shown in Figure 5. The experimental results obtained after optimization in Figure 6b–d demonstrate that the optimized sensor structure provides greatly enhanced measurement performance. Figure 6b indicates that the measurement error obtained over the full range of the optimized sensor was reduced to no more than $2.5 \mu\text{m}$. Moreover, Figure 6c indicates that the error obtained over a 4 mm period was reduced to no more than $\pm 0.25 \mu\text{m}$. Finally, Figure 6d indicates that the first-order harmonic error was greatly reduced from greater than $0.5 \mu\text{m}$ to about $0.05 \mu\text{m}$.

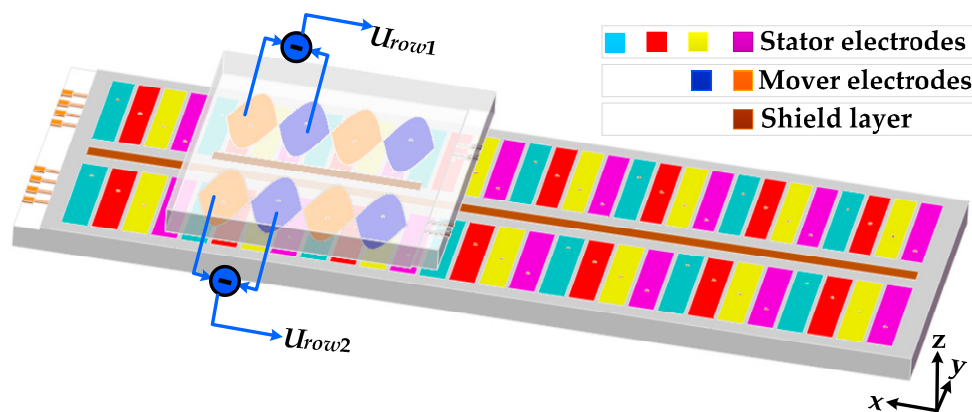


Figure 7. Schematic diagram illustrating the optimized structure of the VATG sensor, which includes increasing the distance between the two rows and adding a shielding layer between them to reduce the influence of signal crosstalk. In addition, a differential induction structure is adopted to reduce common mode disturbance.

5. Conclusions

The present work addressed the limitations of absolute capacitive grating sensors by developing a novel VATG sensor that employs a double-row capacitive structure based on a previously proposed single-row capacitive sensing structure. One capacitor row is composed of n periods over the total sensor length and serves as a fine measurement scale analogous to the auxiliary scale of vernier calipers. The other row is composed of $n - 1$ periods over the total sensor length as a coarse measurement scale analogous to the main scale of vernier calipers. A prototype VATG sensor with a total length of 600 mm was fabricated using PCB manufacturing technology with a fine measurement capacitor row composed of 150 periods and course measurement capacitor row composed of 149 periods. Based on an analysis of the measurement performance of the prototype VATG sensor, the sensor design was optimized by increasing the distance between the two rows and adding a shielding layer between them to reduce the influence of signal crosstalk, and a differential induction structure was adopted to reduce common mode disturbance, which significantly improved the measurement performance of the sensor. Experimental results demonstrated that the measurement error of the optimized prototype sensor was $\pm 1.25 \mu\text{m}$ over the full 600 mm range, $\pm 0.25 \mu\text{m}$ over a single 4 mm period, and the first-order harmonic error was very small.

Author Contributions: Conceptualization, X.L.; Writing and preparation of original draft, H.Z.; Methodology, K.P.; Validation, Q.T. and Z.C.

Funding: This work was funded by the National Natural Science Foundation of China (Grant No. 51435002), by the National Natural Science Foundation of China (Grant No. 51605062), by the University Innovation Team of Chongqing (Grant No. CXTDX201601029), and by the Science and Technology Research Program of Chongqing Municipal Education Commission (Grant No. KJQN201801127).

Acknowledgments: The authors would like to thank Engineering Research Center of Mechanical Testing Technology and Equipment (Ministry of Education), for equipment support services.

Conflicts of Interest: The authors have no conflicts of interest to declare.

References

1. Kai, T.; Akiyama, M.; Nakamura, Y.; Wakui, S. Effects of Back Electromotive Force in an Absolute Displacement Sensor and Improvement Using Current-feedback-type Driver. In *Proceedings of the 2011 International Conference on Advanced Mechatronic Systems*; IEEE: Zhengzhou, China, August 2011; p. 78.
2. Bai, Y.; Lu, Y.; Hu, P.; Wang, G.; Xu, J.; Zeng, T.; Li, Z.; Zhang, Z.; Tan, J. Absolute Position Sensing Based on a Robust Differential Capacitive Sensor with a Grounded Shield Window. *Sensors* **2016**, *16*, 680. [[CrossRef](#)] [[PubMed](#)]

3. Liu, X.; Peng, K.; Chen, Z.; Pu, H.; Yu, Z. A New Capacitive Displacement Sensor with Nanometer Accuracy and Long Range. *IEEE Sens. J.* **2016**, *16*, 2306–2316.
4. Fleming, A.J. A Review of Nanometer Resolution Position Sensors: Operation and performance. *Sens. Actuators A Phys.* **2013**, *190*, 106–126. [[CrossRef](#)]
5. Lin, C.Y.; Lee, C.H. Remote Servo Tuning System for Multi-Axis CNC Machine Tools Using a Virtual Machine Tool Approach. *Appl. Sci.* **2017**, *7*, 776. [[CrossRef](#)]
6. Li, K.; Zhang, Y.; Wei, S.; Yue, H. Evolutionary Algorithm-Based Friction Feedforward Compensation for a Pneumatic Rotary Actuator Servo System. *Appl. Sci.* **2018**, *8*, 1623. [[CrossRef](#)]
7. Bahn, W.; Nam, J.H.; Lee, S.H.; Cho, D.I.D. Digital Optoelectrical Pulse Method for Vernier-Type Rotary Encoders. *IEEE Trans. Instrum. Meas.* **2016**, *65*, 431–440. [[CrossRef](#)]
8. Zhang, Z.; Ni, F.; Dong, Y.; Guo, C.; Jin, M.; Liu, H. A Novel Absolute Magnetic Rotary Sensor. *IEEE Trans. Ind. Electron.* **2015**, *62*, 4408–4419. [[CrossRef](#)]
9. Cai, N.; Xie, W.; Peng, H.; Wang, H.; Yang, Z.; Chen, X. A Novel Error Compensation Method for an Absolute Optical Encoder Based on Empirical Mode Decomposition. *Mech. Syst. Signal Process.* **2017**, *88*, 81–88. [[CrossRef](#)]
10. Girao, P.M.B.S.; Postolache, O.A.; Faria, J.A.B.; Pereira, J.M.C.D. An Overview and a Contribution to the Optical Measurement of Linear Displacement. *IEEE Sens. J.* **2001**, *1*, 322–331. [[CrossRef](#)]
11. Fleming, W.J. Overview of Automotive Sensors. *IEEE Sens. J.* **2002**, *1*, 296–308. [[CrossRef](#)]
12. Xiaokang, L.; Hongji, P.; Fangyan, Z.; Jiqin, F.; Zhicheng, Y. Research on electric field distribution and error characteristics of the nanometer time grating displacement sensor. *Chin. J. Sci. Instrum.* **2013**, *34*, 2257–2264.
13. Friedland, I.; Gurwich, I.; Brandes, A. absolute optical sensors, positioners, optical linear sensor, linear displacement, sensor volt-displacement characteristic, absolute position sensor, sensor scale factor. *Sens. Transducers J.* **2009**, *100*, 125–136.
14. Gage, S.; Evans, D.; Hodapp, M.; Sorensen, H.; Jamison, D.; Krause, B. *Optoelectronics/Fiber-Optics Applications Manual*, 2nd ed.; McGraw-Hill Book Co.: New York, UY, USA, 1981.
15. Hao, S.H.; Liu, J.Z.; Liu, Y.; Hao, M.H.; Song, B.Y. Design of a New Kind of Absolute Magnetic Grid Displacement Sensor. *High Volt. Eng.* **2009**, *35*, 2120–2125.
16. Jiang, K.D. Magnetic flux responsive gate with numerical control system. *Machinery* **2012**, *50*, 39–40.
17. Hao, S.H.; Liu, Y.; Song, B.Y.; Hao, M.H. A Novel Absolute Displacement Detecting Magnetic Sensor. *J. Harbin Inst. Technol.* **2011**, *18*, 81–85.
18. Smith, P.T.; Vallance, R.R.; Marsh, E.R. Correcting Capacitive Displacement Measurements in Metrology Applications with Cylindrical Artifacts. *Precis. Eng.* **2005**, *29*, 324–335. [[CrossRef](#)]
19. Yu, H.; Zhang, L.; Shen, M. Novel Capacitive Displacement Sensor Based on Interlocking Stator Electrodes with Sequential Commutating Excitation. *Sens. Actuators A Phys.* **2015**, *230*, 94–101. [[CrossRef](#)]
20. Ahn, H.J.; Park, J.H.; Um, C.Y.; Han, D.C. A Disk-type Capacitive Sensor for Five-dimensional Motion Measurements. *Meas. Sci. Technol.* **2008**, *19*, 045202. [[CrossRef](#)]
21. Chen, Z.; Pu, H.; Liu, X.; Peng, D.; Yu, Z. A Time-Grating Sensor for Displacement Measurement with Long Range and Nanometer Accuracy. *IEEE Trans. Instrum. Meas.* **2015**, *64*, 3105–3115. [[CrossRef](#)]
22. Yu, Z.; Peng, K.; Liu, X.; Pu, H.; Chen, Z. A New Capacitive Long-range Displacement Nanometer Sensor with Differential Sensing Structure Based on Time-Grating. *Meas. Sci. Technol.* **2018**, *29*, 054009. [[CrossRef](#)]
23. Peng, K.; Yu, Z.; Liu, X.; Chen, Z.; Pu, H. Features of Capacitive Displacement Sensing that Provide High-accuracy Measurements with Reduced Manufacturing Precision. *IEEE Trans. Ind. Electron.* **2017**, *64*, 7377–7386. [[CrossRef](#)]
24. Pu, H.; Liu, H.; Liu, X.; Peng, K.; Yu, Z. A Novel Capacitive Absolute Positioning Sensor Based on Time Grating with Nanometer Resolution. *Mech. Syst. Signal Process.* **2018**, *104*, 705–715. [[CrossRef](#)]
25. Peng, K.; Liu, X.; Chen, Z.; Yu, Z.; Pu, H. Sensing Mechanism and Error Analysis of a Capacitive Long-range Displacement Nanometer Sensor Based on Time Grating. *IEEE Sens. J.* **2017**, *17*, 1596–1607. [[CrossRef](#)]

